https://doi.org/10.1016/j.camwa.2020.01.024

A shear stress transport incorporated elliptic blending turbulence model applied to near-wall, separated and impinging jet flows and heat transfer

X.L. Yang

College of Civil and Transportation Engineering, Shenzhen University, Shenzhen 518060, P.R. China.

Corresponding authors

Y. Liu*

Research Centre for Fluid-Structure Interactions, Department of Mechanical Engineering, The Hong Kong Polytechnic University, Hung Hom, Kowloon, Hong Kong.

e-mail: yang.liu@polyu.edu.hk

L. Yang

College of Civil and Transportation Engineering, Shenzhen University, Shenzhen 518060, P.R. China.

e-mail: yanglei@szu.edu.cn

A shear stress transport incorporated elliptic blending turbulence model applied to near-wall, separated and impinging jet flows and heat transfer

Abstract: An elliptic blending turbulence model, considering the Shear Stress Transport (SST) characteristics in boundary layer together, is developed and validated. This model consists of four governing equations which have the same forms as those used in our previous *k*-*ω*-*φ*-*α* model (belonging to the elliptic blending turbulence models). The major improvement is that a new turbulent viscosity definition, which inherits the advantages of the elliptic blending turbulence models and the SST turbulence models, is constructed. The new model is applied to near-wall, separated and impinging jet flows and associated convective heat transfer. The computational results are compared with available DNS and experimental data and to those computed using the previously developed *k*-*ω*-*φ*-*α* model and the popular Menter's SST *k*-*ω* model. It is shown that the current new model has similar behaviors with the previously developed *k*-*ω*-*φ*-*α* model for the near wall flow and heat transfer. For separated and impinging jet flows and the associated heat transfer, the current new model yields better results than Menter's SST *k*-*ω* model and our previous *k*-*ω*-*φ*-*α* model.

Keywords: turbulence model; elliptic blending; shear stress transport; separated flow; impinging jet flow; convective heat transfer.

Nomenclature

Greek letters

α Elliptic variable

β , γ , β^*, β_0 Turbulence model coefficients

δ_{99} Thickness of the boundary layer

ε Dissipation rate

ω Specific dissipation rate

κ Von Karman constant

μ , ν Molecular dynamic and kinematic viscosity

μ_t , ν_t Turbulent dynamic and kinematic viscosity

Ω_{ij} Vorticity rate tensor

φ Wall-normal turbulent anisotropy, $\varphi = \overline{v^2} / k$

ρ Density of fluid

σ_d Turbulence model constant

$\sigma_k, \sigma_\omega, \sigma_\varepsilon, \sigma_\varphi$ Turbulent Prandtl numbers

τ, τ_w Shear stress and wall shear stress

θ Mean temperature of the fluid

θ_w Wall temperature

θ_{in} Fluid temperature at inlet

θ^+ The normalized temperature

ζ Turbulence model constant

Latin letters

a_1 Turbulence model constant

B Inlet width of the 2D jet

C_f Skin-friction coefficient

C_p Pressure coefficient

c_p Specific heat of the fluid

$C_{\varepsilon 1}, C^*_{\varepsilon 1}, C_{\varepsilon 2}, C^*_{\varepsilon 2}, C_{\varepsilon 4}, C_{\varepsilon 5}, C_\mu, C_T, C_\eta, C_1, C_2$ Turbulence model parameters

C_D Cross-diffusion term

d, D Diameter of the pipe

D_k, D_k^t Turbulent diffusion of k

f Elliptic relaxation function

f_k, f_ω Damping functions

F_b Blending function

G_k Production of turbulent kinetic energy

H Step height or distance from jet exit to plane

I Turbulent intensity

k Turbulent kinetic energy or thermal conductivity of the fluid

L Turbulence length scale

n Turbulence model constant

Nu Nusselt number

p Pressure or turbulence model constant

Pr, Pr_t Molecular and turbulent Prandtl number

q Heat flux

Re_H Reynolds number based on H

Re_t Turbulent Reynolds number

Re_τ Friction velocity based Reynolds number

S Magnitude of strain rate

S_{ij} Strain rate tensor

t Physical time

T Turbulence time scale

T_{lim} Upper bound of the turbulence time scale

u_i Instantaneous velocity vector

$u_i^{'}$ Velocity fluctuation

u, v, w Velocities along x, y and z directions

U_b Mean velocity of the bulk flow

U_{ref} Velocity of the free stream flow

u^+ Normalized velocity by friction velocity

u_τ Friction velocity, $u_\tau = \sqrt{\tau_w / \rho}$

V_0 Mean velocity on the inlet of the 2D jet

$\overline{v^2}$ Velocity variance scale

x Coordinate in the stream-wise direction

y Wall distance or coordinate in the wall-normal direction

y^+ Non-dimensional wall distance

1. Introduction

Though Large Eddy Simulation (LES) seems more powerful than Reynolds Averaged Navier-Stokes (RANS) on unsteady turbulence simulation, the refined modeling of wall effects in the RANS framework is still an energetic topic currently. Indeed, because resolution of wall structures by LES would require very expensive meshes, the application range of LES is limited just for problems without wall effects or wall-bounded flows with Low Reynolds Number (LRN) and limited domain. In practice, several hybrid RANS-LES approaches are developed and become increasingly popular in recent years[1]. The main advantage of hybrid methodologies is that the wall turbulence is modeled using RANS approach thus the mesh requirement in the near wall region is significantly reduced, leading to an increase of the numerical capacity.

Many types of near-wall RANS model have been used in hybrid RANS-LES approaches, from one equation models to full Reynolds Stress Models (RSM): to name a few, the one-equation Spalart–Allmaras model is chosen in the Delayed Detached Eddy Simulation (DDES) model of Spalart et al. [2]. The two-equation Menter's SST $k-\omega$

model is used in the DDES by Mikhail et al.[3] and the Scale Adaptive Simulation (SAS) developed by Menter and Egorov [4]. The four-equation $\varphi - f$ model of Laurence et al.[5], which is based on the elliptic relaxation approach, is applied in the two velocities hybrid RANS-LES model by Uribe et al.[6]. The Elliptic Blending RSM (EBRSM) model of Manceau and Hanjalic[7] is adopted in the seamless approach of Fadai-Ghotbi et al. [8].

Among them, the SST $k-\omega$ model based hybrid approaches is more popular due to its simplicity and robustness . However, the SST $k-\omega$ model does not have superiority for some type of flows. For example, the SST $k-\omega$ model predicts the separation point much early in the diffuser flow[9, 10]. For the problem of impinging jet flow and heat transfer, the SST $k-\omega$ model is not as good as the turbulence models based on elliptic relaxation or elliptic blending approaches[10, 11]. Consequently, as supplements, it is of importance to develop alternative RANS turbulence models.

On the other hand, both LES and hybrid RANS-LES require unsteady 3D modeling. Actually, it is not necessary to carry out unsteady 3D calculations in some problems with steady characteristics, or with typical 2D or axisymmetric configurations. Under these circumstances, RANS turbulence models with good performance are advantageous.

One attractive type of RANS turbulence models is the elliptic relaxation or elliptic blending based models: the $\overline{v^2} - f$ model[12] and its variants, i.e. the $\varphi - f$ model[5], the BL $-\overline{v^2}/k$ model[9] and the $k-\omega-\varphi-\alpha$ model[10, 13]. These models have inherent superiority for near wall flow because they naturally integrate wall turbulence 'damping' by using the wall-normal fluctuations $\overline{v^2}$ as additional scale, and they have been successful in simulation for impinging jet flow and heat transfer.

The researches on the $\overline{v^2} - f$ model and its variants have been sustained about 30 years, leading to several versions of models. Overall, the developments of the $\overline{v^2} - f$ models can be divided into two categories: one stems from the $k-\varepsilon$ system, another stems from the $k-\omega$ system. The $k-\varepsilon$ system based $\overline{v^2} - f$ models have a major drawback associated with the wall boundary condition of ε, especially the unreasonable initial value of ε [10]. Therefore, as stated by Billard and Laurence [9] that it is difficult to give considerations to both stability and accuracy. The $k-\omega$ system based $\overline{v^2} - f$ models can eliminate the disadvantageous effect of the boundary condition and enhance the stability of the models [10, 13, 14]. Recently, the authors developed a $k-\omega-\varphi-\alpha$ model based on the Wilcox's $k-\omega$ model and the BL $-\overline{v^2}/k$ model and applied it

successfully to the near wall and separated flows[10]. Later, the model was further improved (referred to as the $k-\omega-\varphi-\alpha-2018$ model later) and applied successfully to impinging jet flow and heat transfer[13].

In this study, we extend our effort to devise a more robust model, which inherits the advantages of the $k-\omega-\varphi-\alpha-2018$ model and the SST $k-\omega$ model. In the next section, the proposal of the new model is presented in detail. This is followed by the presentation of the solution procedure of the model. Then its performances are verified by comparing with the $k-\omega-\varphi-\alpha-2018$ model and the SST $k-\omega$ model through testing with two dimensional and axisymmetric configurations. Several typical cases have been successfully considered, including the near wall flow, the separated flow and the impinging jet flow. Additionally, the new model is applied to the simulation of heat transfer and shows superior abilities. Finally, some conclusions are drawn.

2. Numerical model

In the RANS framework, for incompressible flow, the mean flow satisfies the RANS equations:

$$\frac{\partial}{\partial x_i}(\rho u_i)=0, \tag{1}$$

$$\frac{\partial \rho u_i}{\partial t}+\frac{\partial}{\partial x_j}\left(\rho u_i u_j\right)=-\frac{\partial p}{\partial x_i}+\frac{\partial}{\partial x_j}\left[\mu\left(\frac{\partial u_i}{\partial x_j}+\frac{\partial u_j}{\partial x_i}\right)-\rho\overline{u_i^{'}u_j^{'}}\right]. \tag{2}$$

For eddy viscosity models, the turbulent stresses are assumed to be linearly proportional to the strain rate and are calculated using

$$-\rho\overline{u_i^{'}u_j^{'}}=\mu_t\left(\frac{\partial u_i}{\partial x_j}+\frac{\partial u_j}{\partial x_i}\right)-\frac{2}{3}\rho k\delta_{ij}, \tag{3}$$

where the eddy viscosity, μ_t, in turn, is calculated using turbulence models.

2.1 Formulation of the present turbulent model

The present turbulent model can be considered as an enhanced version of the $k-\omega-\varphi-\alpha-2018$ model and they have the same governing equations (refer to Yang and Liu[13] and Appendix A). To avoid repetition, they are not described here.

The major improvement of the present model is that it incorporates the shear stress transport characteristics in the boundary layer to the model. The Menter's SST $k-\omega$ model has been proved to be more accurate and reliable for a wider class of flows (for example, adverse pressure gradient flows, airfoils, transonic shock waves) than the standard and the baseline $k-\omega$ models. The reason is that the SST $k-\omega$ model successfully accounts for the transport of the turbulence shear stress in the definition of

the turbulent viscosity. It is acknowledged that the $\overline{v^2}-f$ model and its variants are superior in near wall region, whereas the SST $k-\omega$ model is superior elsewhere. Accordingly, the turbulent viscosity in present model is defined as

$$\mu_t = \left(1-\alpha^p\right) C_\mu \rho \varphi k \min(T, T_{\lim}) + \alpha^p \frac{a_1 \rho k}{\max\left(a_1\omega, F_2 S\right)}, \tag{4}$$

where a_1 is a constant and F_2 is a blending function, as the same used in the SST $k-\omega$ model. In this definition, the first term on the right hand side is coming from the $k-\omega-\varphi-\alpha-2018$ model and the second term is from the SST $k-\omega$ model. A blending function, α^p, is used to achieve a smooth transition from $k-\omega-\varphi-\alpha-2018$ model used in near wall region to SST $k-\omega$ model used elsewhere. This blending formulation inherits the advantages of the $k-\omega-\varphi-\alpha-2018$ model and the SST $k-\omega$ model.

Another modification is the model coefficient σ_k. It is a constant in the $k-\omega-\varphi-\alpha-2018$ model but in present model it is replaced by a blending formulation

$$\sigma_k = \left(1-\alpha^p\right)\sigma_{k1} + \alpha^p \sigma_{k2}. \tag{5}$$

This blending formulation can improve significantly the performance of the model for impinging jet flow with moderate distance from nozzle to plate (as seen in Fig. 20).

The last modification is the production of the kinetic energy, G_k. In the $k-\omega-\varphi-\alpha-2018$ model, it has been shown that using a blending formulation can yield better results [13]. That is, in the near wall region the correction of Kato and Launder [15] is used, i.e.

$$G_k = \mu_t S Q. \tag{6}$$

In other regions, the conventional formula is used. i.e.

$$G_k = \mu_t S^2. \tag{7}$$

However, in present model, it is found that the correction of Kato and Launder [15] works well for whole flow region, thus, Eq. (7) is used to calculate the production of the kinetic energy.

Although most model constants do not require any recalibration from the values given in the $k-\omega-\varphi-\alpha-2018$ model, a few model constants are needed to recalibrate to ensure good performance of the new model. For sake of clarity, the complete equations and constants of the present model are recalled in Appendix A.

It is obvious that the present model does not introduce any additional terms that may result in numerical difficulty. Consequently, the present model has good numerical stability as the $k-\omega-\varphi-\alpha-2018$ model.

2.2 Energy equation and the turbulent Prandtl number

For incompressible flow, the governing equation of the energy can be simplified to the mean temperature (θ) equation. After using the Boussinesq approximation, the unknown eddy diffusivity of heat can be modeled by defining a turbulent Prandtl number, Pr_t. The governing equation of mean temperature can be expressed as

$$\frac{\partial \rho\theta}{\partial t}+\frac{\partial}{\partial x_i}\left(\rho u_i\theta\right)=\frac{\partial}{\partial x_j}\left[\left(\frac{\mu}{\mathrm{Pr}}+\frac{\mu_t}{\mathrm{Pr}_t}\right)\frac{\partial\theta}{\partial x_j}\right], \tag{8}$$

where $\mathrm{Pr}=\mu c_p/k$ represents the molecular Prandtl number.

The turbulent Prandtl number Pr_t depends on several factors, e.g., the molecular Prandtl number of the fluid, the viscosity of the fluid, and the Reynolds number of the flow[16]. There are substantial DNS and experimental data on the Pr_t for 2D channel air flow. Based on the shape of the temperature in the log-layer of the boundary layer, the Pr_t can be assumed to be constant. However, there are no universal values of Pr_t, even in the simple wall shear flows. For example, for air flow with Pr = 0.71, the Pr_t ranges between 0.73 and 0.92 [16].

For fully developed channel flow, Kays and Crawford [17] proposed a formula for Pr_t as

$$\mathrm{Pr}_t=\frac{1}{0.5882+0.228\left(\nu_t/\nu\right)-0.0441\left(\nu_t/\nu\right)^2\left[1-\exp\left(-5.165\nu/\nu_t\right)\right]}. \tag{9}$$

This formula yields a value of 1.7 at the wall and decreases asymptotically to a value of 0.85 far from the wall.

Although the Kays and Crawford formula (Eq. (9)) provides a better shape for the Pr_t in boundary layer, it does not always yield better heat transfer predictions in complex flows. Generally speaking, different type of flows require different Pr_t[13]. However, investigation of the effects of Pr_t is out of the major objective of present study. For the purpose of convenience, the results presented in present paper are all obtained using the Kays and Crawford formula.

3 Solution procedure

The $k-\omega-\varphi-\alpha-2018$ model and the popular SST $k-\omega$ model[18] are used to comparatively display the ability and the superiority of the present model. All computations have been performed using the FLUENT CFD code. The present model and the $k-\omega-\varphi-\alpha-2018$ model are both implemented using the User-Defined Function (UDF) functionality. The SST $k-\omega$ model is an inner-coded turbulence model in FLUENT and so it can be used directly.

The numerical method is the same as that used by Yang and Liu [13]. For the

purpose of clarity, it is also described here briefly. The pressure-based segregated algorithm is used to solve the governing equations. The convection terms in the momentum, energy and turbulence equations are all discretized by the second order upwind scheme. The least squares cell-based method is adopted to evaluate the gradients and derivatives. The SIMPLEC algorithm is used to deal with the velocity-pressure coupling process at the early stage of iteration then switches to the Coupled algorithm. The default under-relaxation factors are adopted for the pressure and velocities. For variables in the turbulence model, under-relaxation factors are set to be different values depending on the complexity of the flow, for example, 0.8 for the near wall and separated flows, and 0.5 for the impinging jet flow.

The no-slip condition is used on solid walls, namely, $u_i = 0$, $k = 0$, $\varphi = 0$, $\alpha = 0$. For ω both in the present model and the $k-\omega-\varphi-\alpha-2018$ model, $\omega_w = 3\nu/(\beta_0 y_1^2)$ is used [10, 13] with y_1 representing the distance from the wall to the centre of the first cell adjacent to the wall. It is different with that used in the SST $k-\omega$ model, in which $\omega_w = 6\nu/(\beta_1 y_1^2)$ is used. The thermal condition on solid wall may be specified to be adiabatic, constant temperature or constant heat flux, to consist with the problem requirements. A zero gradient condition is applied at the outlet that is not periodic in the streamwise direction, for all variables, except pressure. The inlet condition is strongly problem dependent so that it will be stated in each case later. It should be noted that, in all cases, the condition of $y^+ < 1$ is always ensured at the first grid point adjacent to the wall.

4 Results and discussion

Compared with the $k-\omega-\varphi-\alpha-2018$ model and the SST $k-\omega$ model, the ability of the present model for predicting the fluid flow and the heat transfer is evaluated for several test cases. It should be noted that the LRN correction is not included in the SST $k-\omega$ model because this correction may produce a delayed onset of the laminar-turbulent transition and deteriorate the prediction of the model for impinging jet flow, as shown in Yang and Liu[13]. In all cases in present study, Pr = 0.71.

4.1 Near wall flow

Because there are many published available DNS data in literatures, the fully developed turbulent 2D channel flow and axisymmetric pipe flow have been widely used for scrutinizing the near-wall behaviors of turbulence models. For 2D channel flow, four cases with different friction Reynolds number (Re_τ = 180, 550, 2000 and 5200) are chosen for the comparison of fluid flow. The adopted DNS data, provided by Lee and Moser[19], are available online at http://turbulence.ices.utexas.edu. Two friction

Reynolds number (Re_τ = 395 and 1020) are chosen for the comparison of heat transfer. The corresponding DNS data are extracted from Abe et al.[20]. For axisymmetric pipe flow, four cases with different friction Reynolds number (Re_τ = 180, 360, 550 and 1000) are chosen for the comparison of fluid flow. The reference DNS data are extracted from Khoury et al.[21]. Two friction Reynolds number (Re_τ = 180 and 1050) are chosen for comparison of heat transfer. The DNS data come from Saha et al.[22] and Satake et al.[23], respectively. At the inlet, the periodic boundary condition is used for fluid flow and the constant temperature condition is used for heat transfer. On walls, the constant heat flux condition is applied.

The mean streamwise velocity (normalized by friction velocity as $u^+ = u/u_\tau$) profiles for the 2D channel flow are shown in Figure 1. It can be seen that, for all cases, the velocity profiles computed form the present model and the $k-\omega-\varphi-\alpha-2018$ model are almost undistinguishable and in excellent agreement with the DNS data. Apparently, the SST $k-\omega$ model under-predicts the velocity both in the buffer layer and the defect layer, especially in the low Re_τ case.

The good prediction for velocity profiles results from a better scaling of the eddy viscosity. Detailed analysis can be found in Yang and Liu[13]. Figure 2 shows the normalized turbulent viscosity ($\nu^+ = \nu_t/\nu$) profiles. The results from the present model and the $k-\omega-\varphi-\alpha-2018$ model are similar and in good agreement with the DNS data. Particularly, in the defect layer, they predict reasonable structure of the turbulent viscosity, whereas the SST $k-\omega$ model over-predicts the turbulent viscosity dramatically, thus under-predicting the velocity profile.

The normalized temperature ($\theta^+ = (\theta_w - \theta)\rho c_p u_\tau / h$) profiles computed using different turbulence models are compared in Figure 3. It can be seen that the present model and the $k-\omega-\varphi-\alpha-2018$ model predict similar temperature profiles. They are both in good agreement with the DNS data. The SST $k-\omega$ model under-predicts slightly the temperature in the buffer layer and the defect layer.

Figure 4 shows the normalized mean streamwise velocity profiles for the pipe flow. Comparing with the DNS data, the present model and the $k-\omega-\varphi-\alpha-2018$ model can predict velocity profiles very well. The SST $k-\omega$ model under-predicts the velocity profile in the buffer layer and the defect layer significantly. It is obvious that the smaller the Reynolds number, the worse the result. This is not surprised because the SST $k-\omega$ model used in present work does not include the LRN correction, so that it is only appropriate for High Reynolds Number (HRN) flow.

Figure 5 shows the non-dimensional turbulent viscosity profiles for the pipe flow.

Similar to the 2D channel flow (Figure 3), the results predicted by the present model and the $k-\omega-\varphi-\alpha-2018$ model are in good agreement with the DNS data, whereas the SST $k-\omega$ model over-predicts the turbulent viscosity dramatically in the defect layer.

Figure 6 shows the non-dimensional temperature profiles for the pipe flow. In the LRN case (Re_τ = 180), the present model yields the best result compared with the DNS data. The $k-\omega-\varphi-\alpha-2018$ model over-predicts the temperature in the defect layer slightly. It should be noted that the SST $k-\omega$ model, which under-predicts significantly the velocity in this case (Figure 4), predicts strangely the temperature well. The reason may be that the temperature is not only dependent on velocity profile, but also dependent on other quantities (such as the viscosity and the Prandtl number). In the high Reynolds number case (Re_τ = 1050), three turbulent models can predict good temperature profiles both in the viscous sublayer and the log-layer. In the defect layer, the results predicted by the present model and the $k-\omega-\varphi-\alpha-2018$ model are similar and in good agreement with the DNS data, whereas the SST $k-\omega$ model under-predicts it dramatically.

4.2 Separated flow

The 2D backward-facing step flow and the sudden expansion pipe flow (both are abbreviated as step flow later) are selected most frequently as benchmarks for turbulence model validation because they have simple geometries but abundant flow phenomena, such as flow separation, recirculation, reattachment and redevelopment.

The experiment of Vogel and Eaton[24] is used to test the performance of turbulence models for 2D separated flow. The sketch of the geometry and the relevant boundary conditions of the computational model are shown in Figure 7. The horizontal size of computational model is $-3.8H \le x \le 20H$, where H is the step height. The origin of the coordinate system is located at the intersection of the step wall and the bottom wall. The expansion ratio of the test section is 1.25. The inflow conditions, which are extracted from a separated simulation, coincide with the experimental conditions (the boundary layer thickness $\delta_{99} = 1.1H$ at the location of $x = -3.8H$). The temperature is uniform at inlet. On the bottom wall, a constant heat flux condition is applied. On other walls, the adiabatic condition is adopted. The static pressure is set to be constant at outlet. The Reynolds number, Re_H, based on the step height H and the free stream velocity, U_{ref}, is 28000. The number of computational meshes is 302500, which is enough to provide grid-independent solutions.

The distributions of the skin friction coefficient (defined as $C_f = 2\tau_w/(\rho U_{ref}^2)$),

along the bottom wall, computed using different turbulence models, are compared with the experimental measurements in Figure 8. It shows that all three turbulence models can predict the reattachment point (≈ 6.67H) accurately. However, they under-predict C_f in the redevelopment region remarkably. Comparatively speaking, in the separated region, the SST $k-\omega$ model provides better result. In the redevelopment region, the result from the present model is better.

Figure 9 shows the normalized streamwise velocity (u/U_{ref}) profiles on several planes perpendicular to the bottom wall. It shows that the difference among three models is very small and all three turbulence models can yield good results compared with the experiments.

Figure 10 shows the distribution of the local Stanton number (defined as $\mathrm{St} = q/[\rho c_p U_{ref}(\theta_w - \theta_{in})]$) along the bottom wall. Similar to C_f, the SST $k-\omega$ model provides better result in the separated region and the present model provides better result in the redevelopment region.

Similar problem in axisymmetric configuration is the flow in a sudden expansion pipe. In present study, the experiments of Baughn et al.[25, 26] are used to test the performance of turbulence models for axisymmetric separated flow. Figure 11 shows the sketch of the geometry and the relevant boundary conditions of the computational model. The coordinate system is as shown in Figure 11. The inlet is placed at the location of x = -d and the outlet is placed at x = 25d, where d is the diameter of the upstream pipe. The expansion ratio is D/d = 2.5, where D is the diameter of the downstream pipe. The Reynolds number of the flow, Re_D, based on D and the bulk velocity in the downstream pipe, is 17300. At the inlet, conditions obtained from a separated simulation of fully developed pipe flow using the same turbulence model, are applied. The constant static pressure condition is set to the outlet. For thermal conditions, a uniformly distributed temperature is set at inlet. On the inlet wall and the step wall, the adiabatic condition is adopted. On the side wall, two type conditions are individually considered according to different requirements. Specifically, the constant temperature condition is adopted for the analysis of the temperature distribution (Figure 13) and the constant heat flux condition is applied for the analysis of Nu (Figure 14). The reason is that the measurement of temperature was only carried out with the constant temperature condition[26] and the calculation of Nu in the case with constant heat flux condition[25] (integral can be avoided) is easier than the case with constant temperature condition. The number of computational cells is 137600, which is fine enough to obtain grid independent solutions.

The centerline velocity (along the axis and normalized by the centerline velocity in upstream pipe) is shown in Figure 12. It is obvious that the $k-\omega-\varphi-\alpha-2018$ model

delays the velocity decay significantly. The velocity decay predicted by the present model is in good agreement with the experimental measurement[26]. The SST $k-\omega$ model yields also good result.

The normalized mean temperature profiles (defined as $\theta^+ = (\theta - \theta_{in})/(\theta_w - \theta_{in})$) at several locations in the downstream pipe are compared in Figure 13. Apparently, the temperature profiles computed by three turbulence models are in good agreement with experiments[26]. As a whole, the present model predicts better results.

The local Nusselt number (Nu) on side wall is normalized by the Nusselt number computed using the classic Dittus-Boelter relation for the fully developed pipe flow (Nu_{DB}). Figure 14 shows the comparison of the computed results and the experimental measurement[25]. It can be seen that only the present model can predict the peak value of Nu well, which occurs at the reattachment point. The $k-\omega-\varphi-\alpha-2018$ model and the SST $k-\omega$ model under-predict the peak value.

4.3 Impinging jet flow

Turbulent impinging jet flow is a challenge for turbulence models because it has several complex features (such as free shear, stagnation and high streamline curvature) which are difficult to be predicted. Therefore, this flow is a good vehicle for evaluation of turbulence models. In present study, the plane (2D) impinging jet flow and circular (axisymmetric) impinging jet flow are both considered.

The experiment of Ashforth-Frost et al. [27] is chosen to check the performance of the turbulence models in 2D impinging jet flow. Two cases with different distance from nozzle to plate (H/B = 4 and H/B = 9.2) are considered. The Re (based on the width of the slot, B, and the mean velocity at inlet, V_0) is 20000. The detailed information about the computational model, including the size of the computational domain and the boundary conditions, can be found in Yang and Liu[13]. For the convenience of discussion, the sketch is shown in Figure 15. The number of meshes, 140000 for the case of H/B = 4 and 180000 for the case of H/B = 9.2, are enough to provide grid-independent solutions. The experiment of Zhe and Modi [28] is also included for comparison.

Figure 16 shows the comparison of the x-velocity profiles (normalized by V_0) predicted by all three turbulence models and the experimental data of Ashforth-Frost et al. [27] and Zhe and Modi [28] on different vertical planes perpendicular to the impingement wall in the H/B = 4 case. It can be observed that the present model yields the best velocity profiles on all vertical planes. Only the profiles predicted by the present model have the same shape with those from the experiment of Zhe and Modi [28], although there is a certain degree of difference in value.

The distributions of the Nusselt number (defined as $\mathrm{Nu} = qB/[k(\theta_w - \theta_{in})]$) on the impingement wall in the H/B = 4 case, including those predicted by the three turbulence models and that measured by Ashforth-Frost et al. [27], are compared in Figure 17. Obviously, the result predicted by the present model is better than other models. The Nu distribution predicted by the $k-\omega-\varphi-\alpha-2018$ model agrees fairly well with the experimental result, but that predicted by the SST $k-\omega$ model is not good. It should be noted that the result predicted by the SST $k-\omega$ model in present study is different from that in Yang and Liu[13]. The reason is that the LRN correction is not used in present study but it is used in Yang and Liu[13].

Figure 18 shows the comparison of the x-velocity profiles predicted by all three turbulence models and the experimental data of Ashforth-Frost et al. [27] and Zhe and Modi [28] on different vertical planes in the H/B = 9.2 case. Overall, the present model yields the best velocity profiles on all vertical planes. The $k-\omega-\varphi-\alpha-2018$ model and the SST $k-\omega$ model over-predict dramatically the velocity in the near wall region.

Figure 19 shows the comparison of the Nusselt number distribution on the impingement wall predicted by the three turbulence models and that measured by Ashforth-Frost et al. [27] in the H/B = 9.2 case. Apparently, only the present model is able to generate the steady decrease of the Nu profile as experiment. In contrast, the $k-\omega-\varphi-\alpha-2018$ model and the SST $k-\omega$ model predict false secondary peak for Nu.

It is found that the Nu distribution is affected strongly by σ_k, one of the model coefficients. To demonstrate this, the Nu is recalculated using the present model. Except to set σ_k to be a constant of 0.6 (the same as in the $k-\omega-\varphi-\alpha-2018$ model), other conditions keep unchanged. The results are shown in Figure 20. It illustrates that the false secondary peak occurs when σ_k = 0.6. Consequently, in present model Eq.(5) is used for σ_k.

The problem of a circular jet issuing from a long straight pipe nozzle impinged orthogonally onto a flat plate is chosen to check the performance of the turbulence models in axisymmetric impinging jet flow. Though there are amounts of experiments for this problem, only one case with Re = 23000 and H/D = 2, which means the ratio of the distance from jet exit to plate and the diameter of the circular nozzle, is chosen in present study due to limitations of coverage. To be specific, the experiment of Tummers et al.[29] is used for analysis of the flow dynamic. The experiments of Baughn and Shimizu[30], Baughn et al.[31] and Katti and Prabhu [32] are used for analysis of heat transfer.

The computational model is constructed according to the experimental conditions.

The sketch of the computational domain and the accompanying boundary conditions are shown in Figure 21. The computational domain is a rectangle of 8*D*×10*D*. The length of the nozzle pipe is 6*D*. At inlet, a fully developed turbulent pipe flow is specified. This is achieved by extracting the related quantities from a separated simulation of pipe flow under the same condition. At outlet, the constant pressure condition is applied. A constant heat flux condition is specified on the impingement wall and a constant temperature condition is applied at inlet. On the nozzle wall, the adiabatic condition is adopted. The mesh sensitivity is investigated and it indicates that the number of meshes (260000) used in present study is enough to obtain grid-independent solutions.

The skin friction coefficients C_f (defined as $C_f = 2\tau_w/(\rho U_b^2)$) distributed along the impingement wall, computed using different turbulence models, are compared with the experimental data of Tummers et al.[29] in Figure 22. The difference among three turbulence models occurs mainly in the region of laminar-to-turbulent transition. This result indicates that the three models have different ability to predict laminar-to-turbulent transition.

Figure 23 shows the mean radial velocity (normalized by the bulk velocity of nozzle, U_b) for different wall-normal traverses. For the traverses at r/D = 0.25 and r/D = 0.5, the results predicted by the present model and the $k-\omega-\varphi-\alpha-2018$ model are in good agreement with the experimental results[29], whereas the SST $k-\omega$ model under-predicts the peak near the wall. For the traverses at r/D = 0.75 and r/D = 1, the difference among three models mainly appears in the shear layer. The SST $k-\omega$ model yields better result.

Figure 24 shows the local Nu (defined as $\mathrm{Nu} = qD/[k(\theta_w - \theta_{in})]$) distributed on the impingement wall. It can be seen that the experimental data are scattered to a certain extent. Even so, it is clear that there is a dip within r/D = 1 and r/D = 2, which is followed by a secondary peak within r/D = 2 and r/D = 3. The present model and the $k-\omega-\varphi-\alpha-2018$ model predict the dip and the secondary peak very well comparing with the measured data of Baughn and Shimizu[30] and Baughn et al.[31]. However, the dip and the secondary peak are not well reproduced by the SST $k-\omega$ model. At large distance from the axis (r/D > 2), the Nu profiles predicted by the present model and the $k-\omega-\varphi-\alpha-2018$ model are in good agreement with the experimental data of Baughn and Shimizu[30] and Baughn et al.[31] but the SST $k-\omega$ model under-predicts somewhat the Nu.

Conclusions

An elliptic blending turbulence model is developed incorporating the shear stress transport characteristics and its abilities on simulating fluid flow and heat transfer are tested on several typical flows with 2D and axisymmetric configurations. The calculated results are verified using available DNS and experimental data. The present model is also compared with the $k-\omega-\varphi-\alpha-2018$ model and the SST $k-\omega$ model. The results lead to the following conclusions:

(1) In near wall flow and heat transfer, the results predicted by the present model and the $k-\omega-\varphi-\alpha-2018$ are in good agreement with the DNS data. The SST $k-\omega$ model under-predicts the velocity and temperature profiles in the log-layer and the defect layer to some degree.

(2) In the 2D step flow, three turbulence models yield fairly good results comparing with the experimental measurement. In the axisymmetric step flow, the results predicted by the present model are in good agreement with experiments. Whereas the $k-\omega-\varphi-\alpha-2008$ model delays significantly the velocity decay at the centerline, and it cannot predict the peak of Nu on the side wall.

(3) In the impinging jet flow and heat transfer, the present model yield the best results for all cases. In the 2D case with small distance between jet exit and impingement wall (H/B = 4.0), the velocity profiles predicted by the SST $k-\omega$ model are better than those predicted by the $k-\omega-\varphi-\alpha-2008$ model. In contrast, the local Nu distribution predicted by $k-\omega-\varphi-\alpha-2008$ model is better than that computed by the SST $k-\omega$ model. In the 2D case with moderate distance (H/B = 9.2), both of the $k-\omega-\varphi-\alpha-2008$ model and the SST $k-\omega$ model fail to predict the local Nu distribution.

Acknowledgements

Support given by the National Natural Science Foundation of China (Project No. 51678364) and The Hong Kong Polytechnic University under grant No. G-UACM is gratefully acknowledged.

Appendix A: Formulation of the present model

The equations of the present model are summarized below.

$$\frac{\partial \rho k}{\partial t}+\frac{\partial}{\partial x_i}(\rho u_i k)=G_k-\rho f_k \beta^* k\omega+\frac{\partial}{\partial x_j}\left[\left(\frac{\mu}{2}+\sigma_k \mu_t\right)\frac{\partial k}{\partial x_j}\right] \tag{A.1}$$

$$\frac{\partial \rho \omega}{\partial t}+\frac{\partial}{\partial x_i}(\rho u_i \omega)=f_\omega \gamma \frac{\omega}{k}G_k-\rho\beta\omega^2+C_D+\frac{\partial}{\partial x_j}\left[\left(\frac{\mu}{2}+\sigma_\omega \mu_t\right)\frac{\partial \omega}{\partial x_j}\right] \tag{A.2}$$

$$\frac{\partial \rho \varphi}{\partial t}+\frac{\partial}{\partial x_i}(\rho u_i \varphi)=\left(1-\alpha^p\right)\rho f_{wall}+\alpha^p \rho f_{\hom}-\frac{\varphi}{k}G_k+\frac{2}{k}\mu_t\sigma_k\frac{\partial \varphi}{\partial x_j}\frac{\partial k}{\partial x_j}+\frac{\partial}{\partial x_j}\left[\left(\frac{\mu}{2}+\sigma_\varphi \mu_t\right)\frac{\partial \varphi}{\partial x_j}\right] \tag{A.3}$$

$$0=\frac{1-\alpha}{L^2}+\frac{\partial}{\partial x_j}\left(\frac{\partial \alpha}{\partial x_j}\right) \tag{A.4}$$

$$\mu_t=\left(1-\alpha^p\right)C_\mu \rho \varphi k \min(T,T_{\lim})+\alpha^p\frac{a_1 \rho k}{\max(a_1\omega,F_2 S)} \tag{A.5}$$

$$G_k=\mu_t S\Omega \tag{A.6}$$

$$f_{wall}=-\frac{\beta^*\omega\varphi}{2} \tag{A.7}$$

$$f_{\hom}=-\frac{1}{T}\left(C_1-1+C_2\frac{G_k}{\rho\beta^* k\omega}\right)\left(\varphi-\frac{2}{3}\right) \tag{A.8}$$

$$F_2=\tanh(\Phi^2) \tag{A.9}$$

$$\Phi=\max\left(\frac{2\sqrt{k}}{0.09\omega y},\frac{500\mu}{\rho\omega y^2}\right) \tag{A.10}$$

$$\sigma_k=\left(1-\alpha^p\right)\sigma_{k1}+\alpha^p\sigma_{k2} \tag{A.11}$$

$$f_k=[\beta_0/0.27+(\mathrm{Re}_t/8)^4]/[1+(\mathrm{Re}_t/8)^4] \tag{A. 12}$$

$$f_\omega=(2.0+\mathrm{Re}_t/2.61)/(1+\mathrm{Re}_t/2.6) \tag{A.13}$$

$$\beta=(C^*_{\varepsilon 2}-1)\beta^* \tag{A. 14}$$

$$C^*_{\varepsilon 2}=C_{\varepsilon 2}+\alpha^p\left(C_{\varepsilon 4}-C_{\varepsilon 2}\right)\tanh\left[\max\left(\frac{D^t_k}{\beta^* k\omega},0\right)\right] \tag{A. 15}$$

$$D^t_k=\frac{1}{\partial x_i}\left(\nu_t\sigma_k\frac{\partial k}{\partial x_i}\right) \tag{A. 16}$$

$$\gamma = C_{\varepsilon 1}^{*} - 1 \tag{A. 17}$$

$$C_{\varepsilon 1}^{*} = C_{\varepsilon 2} - \kappa^2 \sigma_\omega / \sqrt{\beta^*} - C_{\varepsilon 5} + \frac{C_{\varepsilon 5}}{1 + [C_L y/(2L)]^8} \tag{A. 18}$$

$$C_D = \sigma_d \frac{\rho}{\omega} \max\left(\frac{\partial k}{\partial x_j} \frac{\partial \omega}{\partial x_j}, 0.0 \right) \tag{A. 19}$$

$$\begin{cases} L = C_L \max\left[\dfrac{\sqrt{k}}{\beta^* \omega}, C_\eta \dfrac{\nu^{3/4}}{\left(\beta^* k \omega\right)^{1/4}} \right] \\ T = \max\left[\dfrac{1}{\beta^* \omega}, C_T \dfrac{\nu^{1/2}}{\left(\beta^* k \omega\right)^{1/2}} \right] \end{cases} \tag{A. 20}$$

$$T_{\lim} = \frac{\zeta}{\sqrt{3} C_\mu \varphi S} \tag{A. 21}$$

where $S = \sqrt{2 S_{ij} S_{ij}}$, $S_{ij} = \frac{1}{2}(u_{i,j} + u_{j,i})$, $\Omega = \sqrt{2 \Omega_{ij} \Omega_{jk}}$, $\Omega_{ij} = \frac{1}{2}(u_{i,j} - u_{j,i})$, and y is the distance to the nearest wall.

The model constants extracted directly from $k - \omega - \varphi - \alpha - 2018$ model are listed in Table A.1 and those re-calibrated are listed in Table A.2.

References

[1] P.A. Durbin, Some recent developments in turbulence closure modeling, Annual Review of Fluid Mechanics, 50 (2018) 77-103.

[2] P.R. Spalart, S. Deck, M.L. Shur, K.D. Squires, M.K. Strelets, A. Travin, A new version of detached-eddy simulation, resistant to ambiguous grid densities, Theoretical and Computational Fluid Dynamics, 20 (2006) 181-195.

[3] M.S. Gritskevich, A.V. Garbaruk, J. Schütze, F.R. Menter, Development of DDES and IDDES formulations for the k-ω shear stress transport model, Flow, Turbulence and Combustion, 88 (2012) 431-449.

[4] F.R. Menter, Y. Egorov, The scale-adaptive simulation method for unsteady turbulent flow predictions. Part 1: theory and model description, Flow, Turbulence and Combustion, 85 (2010) 113-138.

[5] D.R. Laurence, J.C. Uribe, S.V. Utyuzhnikov, A robust formulation of the v^2–f model, Flow, Turbulence and Combustion, 73 (2005) 169-185.

[6] J.C. Uribe, N. Jarrin, R. Prosser, D. Laurence, Development of a two-velocities Hybrid RANS-LES model and its application to a trailing edge flow, Flow, Turbulence and Combustion, 85 (2010) 181-197.

[7] R. Manceau, K. Hanjalić, Elliptic blending model: A new near-wall Reynolds-stress turbulence closure, Physics of Fluids, 14 (2002) 744.

[8] A. Fadai-Ghotbi, C. Friess, R. Manceau, T.B. Gatski, J. Borée, Temporal filtering: A consistent formalism for seamless hybrid RANS–LES modeling in inhomogeneous turbulence, International Journal of Heat and Fluid Flow, 31 (2010) 378-389.

[9] F. Billard, D. Laurence, A robust k−ε−v^2/k elliptic blending turbulence model applied to near-wall, separated and buoyant flows, International Journal of Heat and Fluid Flow, 33 (2012) 45-58.

[10] X.L. Yang, L. Yang, Z.W. Huang, Y. Liu, Development of a k–ω–φ–α turbulence model based on elliptic blending and applications for near-wall and separated flows, Journal of Turbulence, 18 (2017) 36-60.

[11] A. Pattamatta, G. Singh, H. Mongia, Assessment of turbulence models for free and confined impinging jet flows, 42nd AIAA Thermophysics Conference, American Institute of Aeronautics and Astronautics, 2011.
[12] P.A. Durbin, Near-wall turbulence closure modeling without damping functions, Theoretical and Computational Fluid Dynamics, 3 (1991) 1-13.
[13] X.L. Yang, Y. Liu, An improved k–ω–φ–α turbulence model applied to near-wall, separated and impinging jet flows and heat transfer, Computers & Mathematics with Applications, 76 (2018) 315-339.
[14] R.M. Jones, Advanced turbulence modeling for industrial flows, Agricultural and Mechanical College, Louisiana State University, 2003.
[15] M. Kato and B. E. Launder, The modelling of turbulent flow around stationary and vibrating square cylinders, Ninth Symposium on "Turbulent Shear Flows". Kyoto, Japan. August 16-18, 1993.
[16] W.M. Kays, Turbulent Prandtl number—where are we? Journal of Heat Transfer, 116 (1994) 284-295.
[17] W.M. Kays, M.E. Crawford, Convective heat and mass transfer, McGraw-Hill Education, New York, 1993.
[18] F.R. Menter, Improved two equation k-ω turbulence models for aerodynamic flows, NASA Technical Memorandum, 1992.
[19] M. Lee, R.D. Moser, Direct numerical simulation of turbulent channel flow up to Re_τ = 5200, Journal of Fluid Mechanics, 774 (2015) 395-415.
[20] H. Abe, H. Kawamura, Y. Matsuo, Surface heat-flux fluctuations in a turbulent channel flow up to Re_τ=1020 with Pr=0.025 and 0.71, International Journal of Heat and Fluid Flow, 25 (2004) 404-419.
[21] G.K. El Khoury, P. Schlatter, A. Noorani, P.F. Fischer, G. Brethouwer, A.V. Johansson, Direct numerical simulation of turbulent pipe flow at moderately high Reynolds numbers, Flow, Turbulence and Combustion, 91 (2013) 475-495.
[22] S. Saha, J.C. Klewicki, A.S.H. Ooi, H.M. Blackburn, Comparison of thermal scaling properties between turbulent pipe and channel flows via DNS, International Journal of Thermal Sciences, 89 (2015) 43-57.
[23] S.-i. Satake, T. Kunugi, R. Himeno, High Reynolds number computation for turbulent heat transfer in a pipe flow, in: J.K. Valero M., Kitsuregawa M., Tanaka H. (Ed.) International Symposium on High Performance Computing, Springer, Berlin, Heidelberg, 2000, pp. 514-523.
[24] J. C. Vogel, J. K. Eaton, Combined heat transfer and fluid dynamic measurements downstream of a backward-facing step, Journal of Heat Transfer, 107 (1985) 922-929.
[25] J. W. Baughn, M. A. Hoffman, R. K. Takahashi, B. Launder, Local heat transfer downstream of an abrupt expansion in a circular channel with constant wall heat flux, Journal of Heat Transfer, 106 (1984) 789-796.
[26] J. W. Baughn, M. A. Hoffman, B. Launder, D. Lee, C. Yap, Heat transfer, temperature, and velocity measurements downstream of an abrupt expansion in a circular tube at a uniform wall temperature, Journal of Heat Transfer, 111 (1989) 870-876.
[27] S. Ashforth-Frost, K. Jambunathan, C.F. Whitney, Velocity and turbulence characteristics of a semiconfined orthogonally impinging slot jet, Experimental Thermal and Fluid Science, 14 (1997) 60-67.
[28] J. Zhe, V. Modi, Near wall measurements for a turbulent impinging slot jet (Data Bank Contribution), Journal of Fluids Engineering, 123 (2001) 112.
[29] M.J. Tummers, J. Jacobse, S.G.J. Voorbrood, Turbulent flow in the near field of a round impinging jet, International Journal of Heat and Mass Transfer, 54 (2011) 4939-4948.
[30] J.W. Baughn, S. Shimizu, Heat transfer measurements from a surface with uniform heat flux and an impinging jet, Journal of Heat Transfer, 111 (1989) 1096-1098.

[31] J.W. Baughn, A.E. Hechanova, X. Yan, An experimental study of entrainment effects on the heat transfer from a flat surface to a heated circular impinging jet, Journal of Heat Transfer, 113 (1991) 1023-1025.
[32] V. Katti, S.V. Prabhu, Experimental study and theoretical analysis of local heat transfer distribution between smooth flat surface and impinging air jet from a circular straight pipe nozzle, International Journal of Heat and Mass Transfer, 51 (2008) 4480-4495.

Table captions

Table A.1. Model constants extracted directly from the $k-\omega-\varphi-\alpha-2018$ model.

Table A.2. Model constants re-calibrated in the present model.

Figure captions

Figure 1. Comparisons of the normalized mean streamwise velocity profiles for 2D channel flow. (a) Re_τ = 180; (b) Re_τ = 550; (c) Re_τ = 2000; (d) Re_τ = 5200.

Figure 2. Comparisons of the normalized turbulent viscosity profiles for 2D channel flow. (a) Re_τ = 180; (b) Re_τ = 550; (c) Re_τ = 2000; (d) Re_τ = 5200.

Figure 3. Comparisons of the normalized temperature profiles for 2D channel flow. (a) Re_τ = 360; (b) Re_τ = 1020.

Figure 4. Comparisons of the normalized mean streamwise velocity profiles for axisymmetric pipe flow. (a) Re_τ = 180; (b) Re_τ = 360; (c) Re_τ = 550; (d) Re_τ = 1000.

Figure 5. Comparisons of the normalized turbulent viscosity profiles for axisymmetric pipe flow. (a) Re_τ = 180; (b) Re_τ = 360; (c) Re_τ = 550; (d) Re_τ = 1000.

Figure 6. Comparisons of the normalized temperature profiles for axisymmetric pipe flow. (a) Re_τ = 180; (b) Re_τ = 1050.

Figure 7. Sketch of the geometry and boundary conditions of the 2D step flow.

Figure 8. Comparison of the skin friction coefficients on the bottom wall of the 2D step flow.

Figure 9. Velocity profiles at different traverses of the 2D step flow.

Figure 10. Comparison of the local Nu on the bottom wall of the 2D step flow.

Figure 11. Sketch of the geometry and boundary conditions of the sudden expansion pipe flow.

Figure 12. Comparison of the *u*-velocity on centerline of the sudden expansion pipe flow.

Figure 13. Comparison of the temperature profiles at different traverses of the sudden expansion pipe flow. (a) x/H = 0.25; (b) x/H = 6; (c) x/H = 10; (d) x/H = 22.

Figure 14. Comparison of the local Nu on the side wall of the sudden expansion pipe flow.

Figure 15. Sketch of the geometry and boundary conditions for the 2D impinging jet flow.

Figure 16. Comparisons of the mean streamwise velocity profiles at different vertical

Tables

Table A.1.

β^*	β_0	σ_ω	κ	p	σ_φ	$C_{\varepsilon 2}$	C_1	C_2	C_T	C_L	C_η
0.09	0.0708	0.5	0.41	4.0	1.0	1.787	1.7	0.9	6.0	0.164	79

Table A.2.

C_μ	$C_{\varepsilon 4}$	$C_{\varepsilon 5}$	σ_d	σ_{k1}	σ_{k2}	ζ	a_1
0.2	1.0	0.23	0.52	0.6	1.1	0.5	0.31

Figures

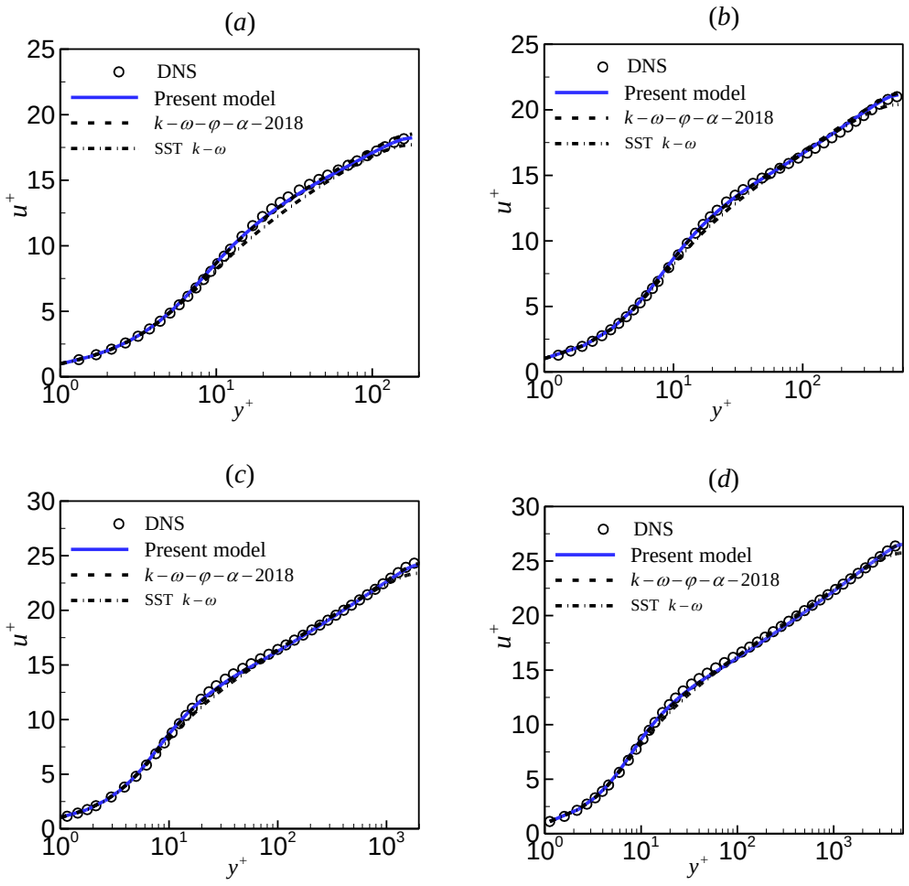

Figure 1.

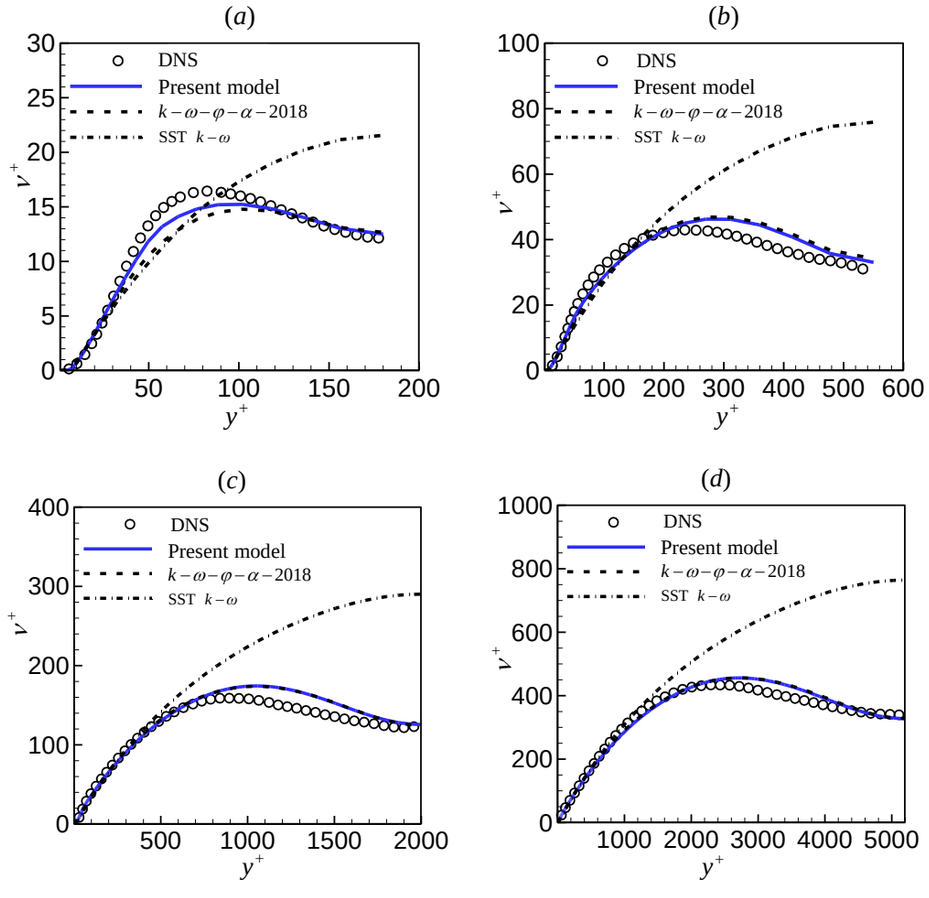

Figure 2.

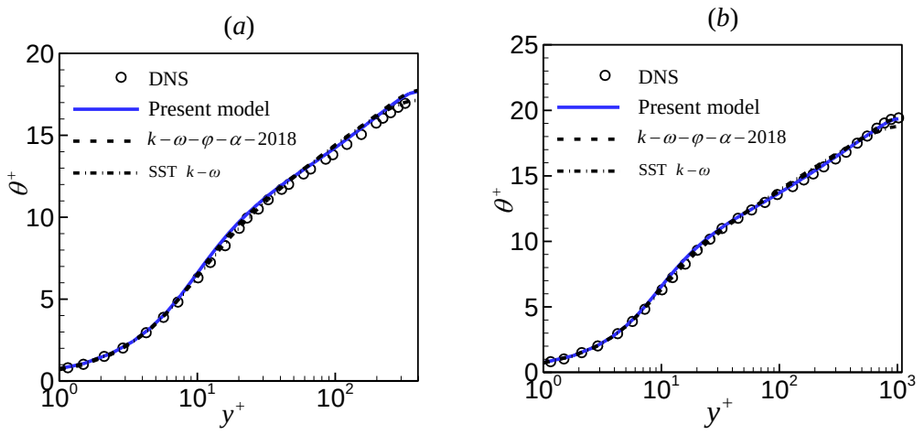

Figure 3.

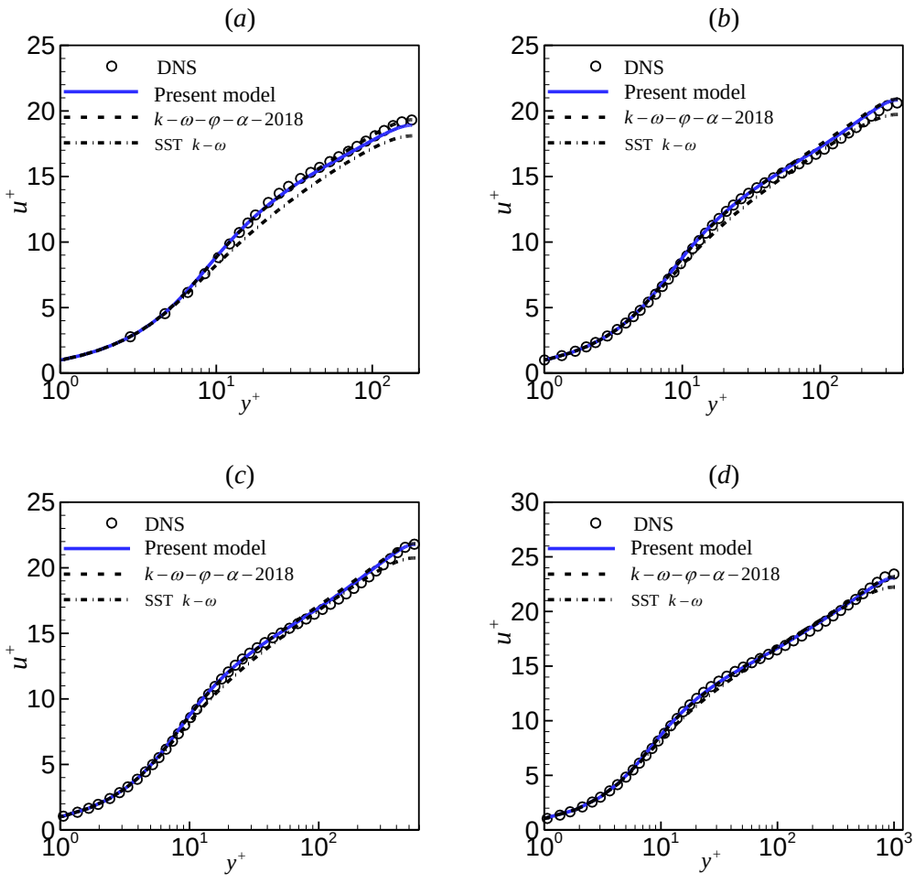

Figure 4.

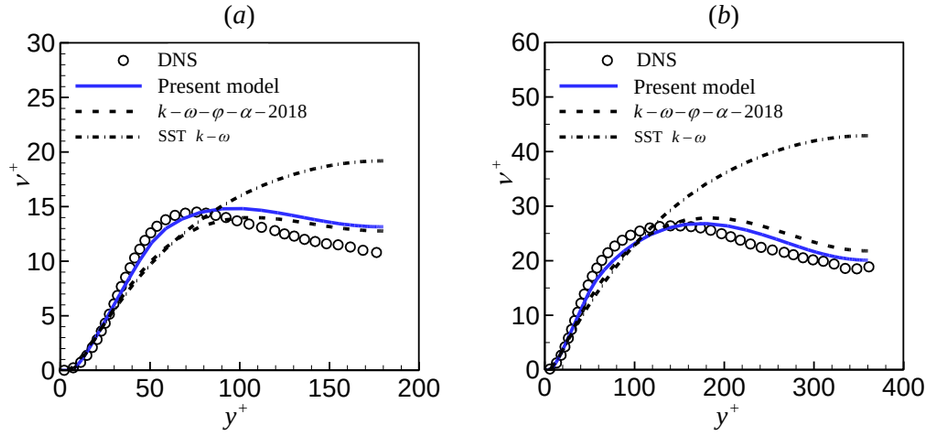

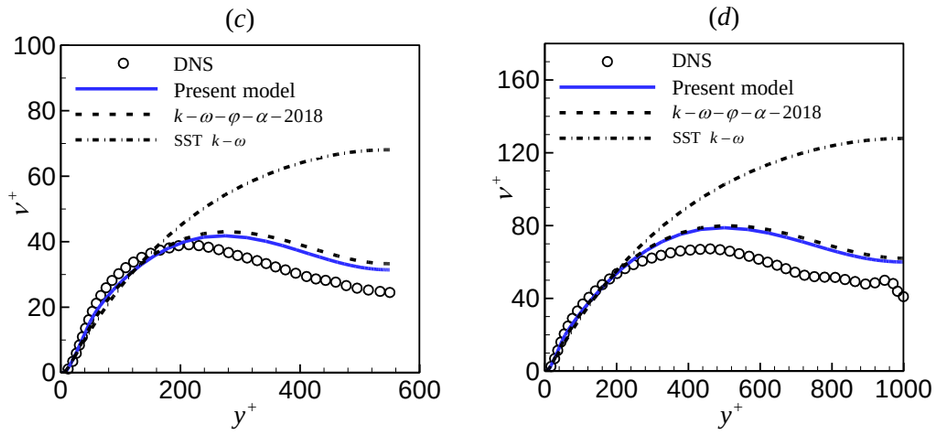

Figure 5.

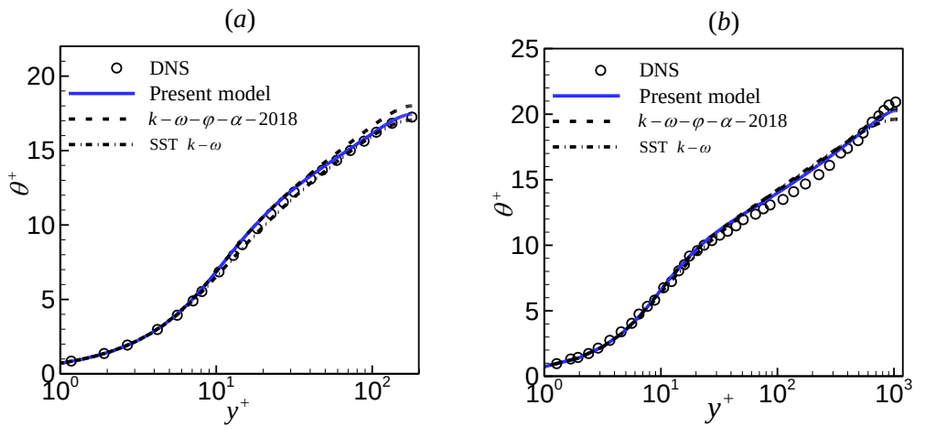

Figure 6

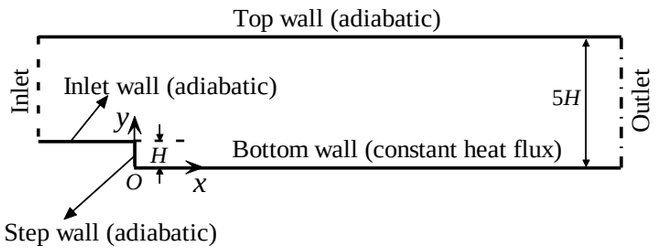

Figure 7.

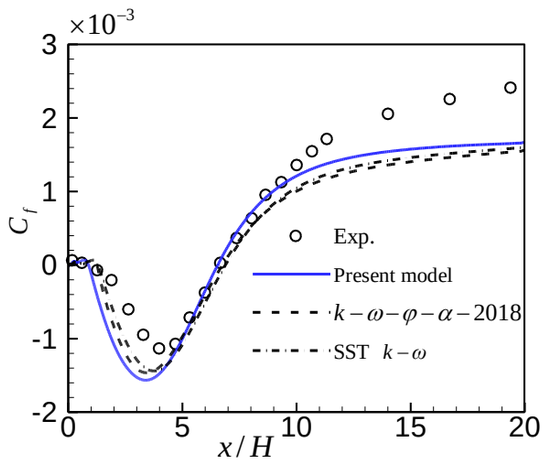

Figure 8.

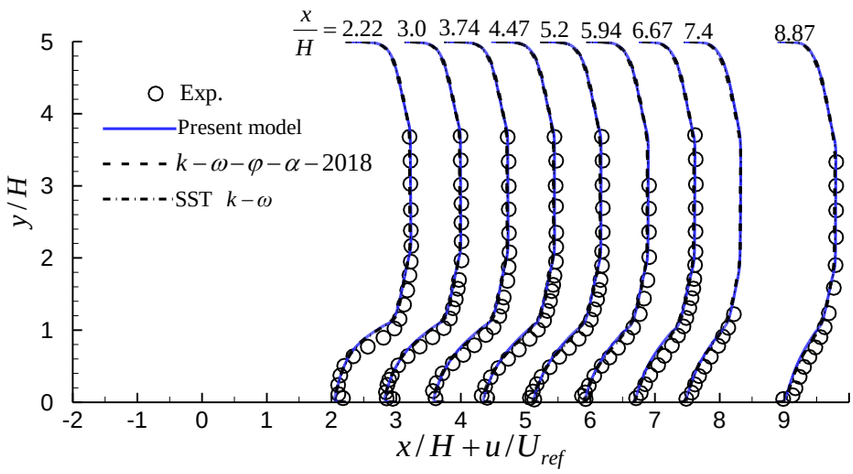

Figure 9.

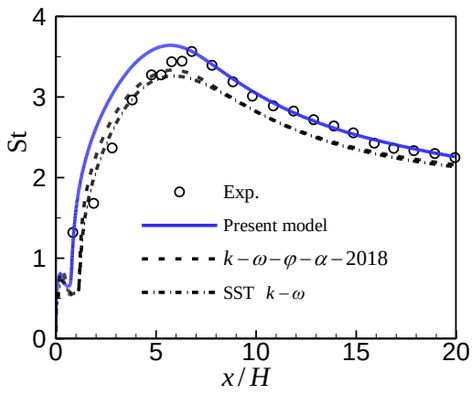

Figure 10.

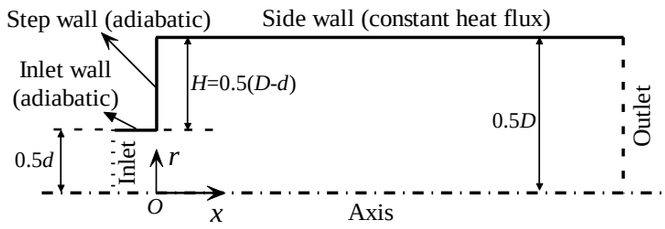

Figure 11.

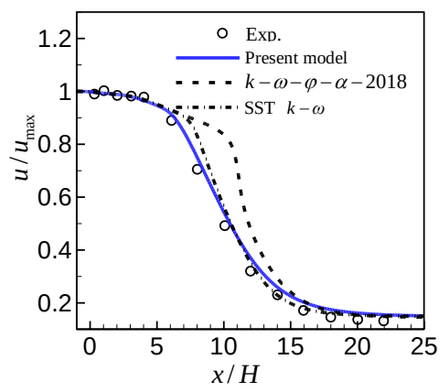

Figure 12.

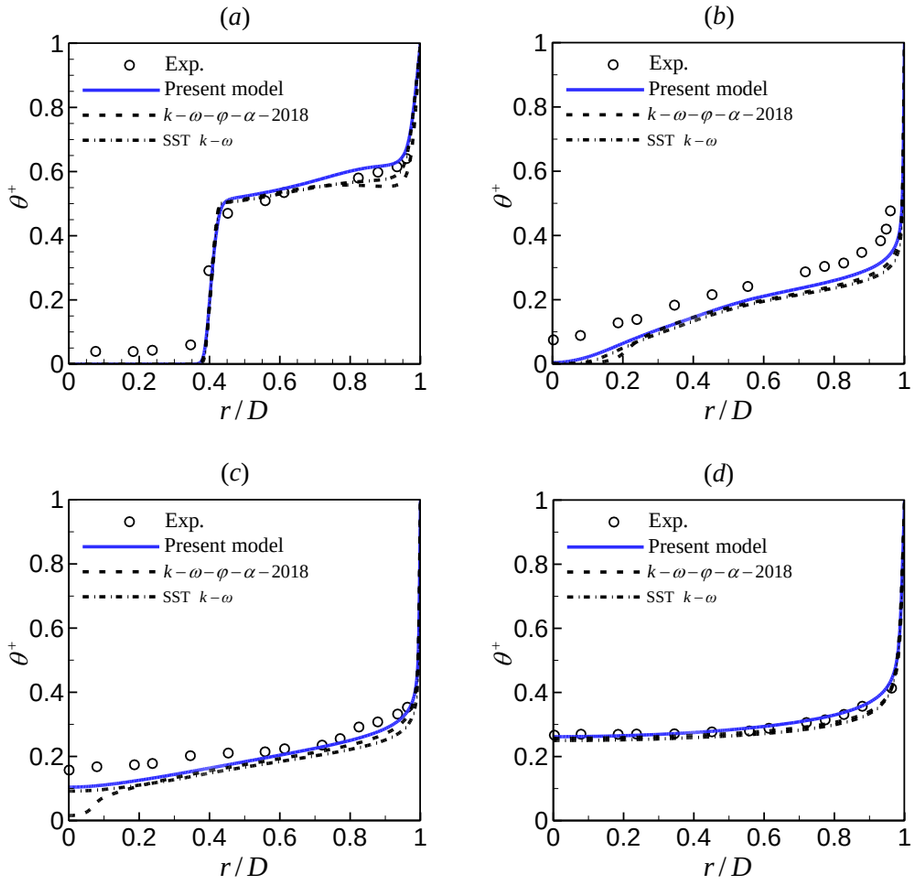

Figure 13.

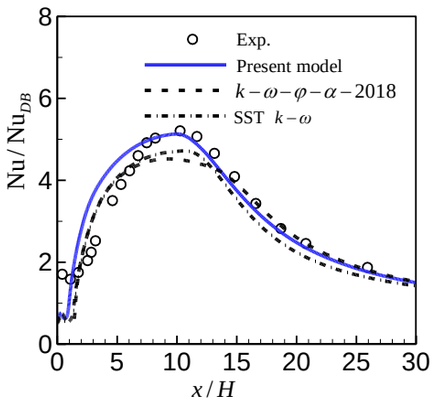

Figure 14.

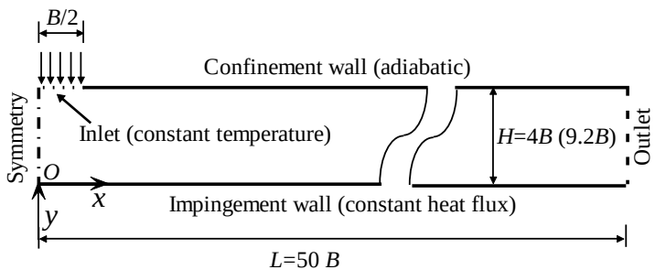

Figure 15.

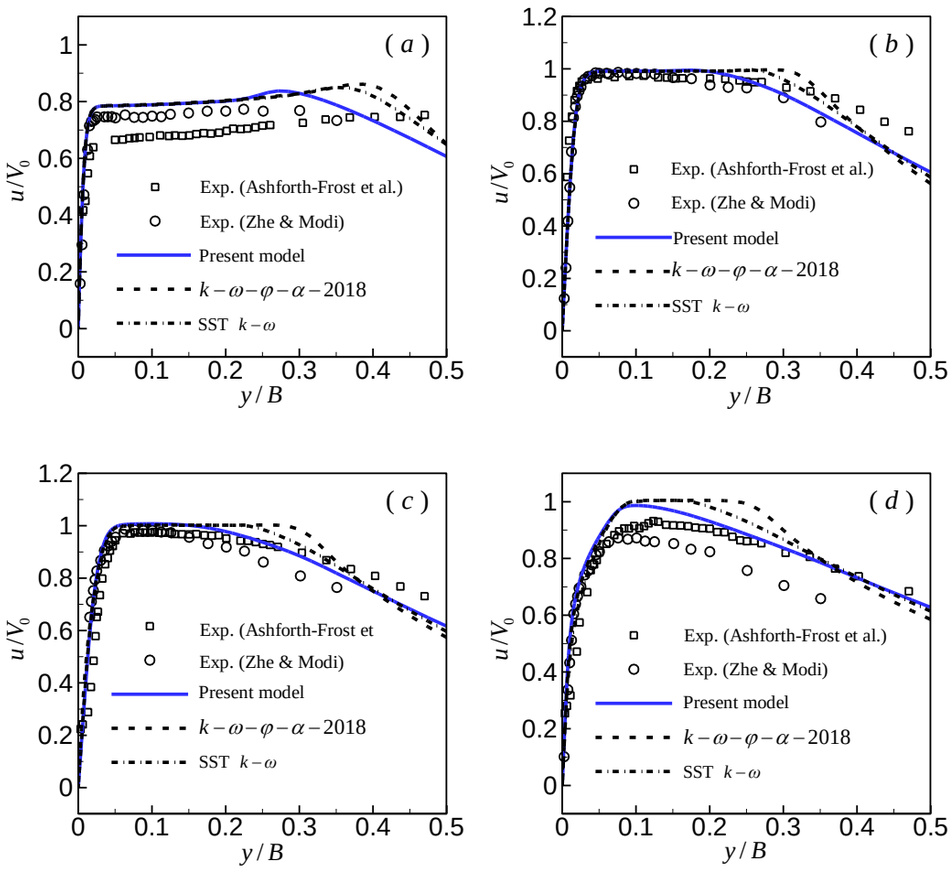

Figure 16.

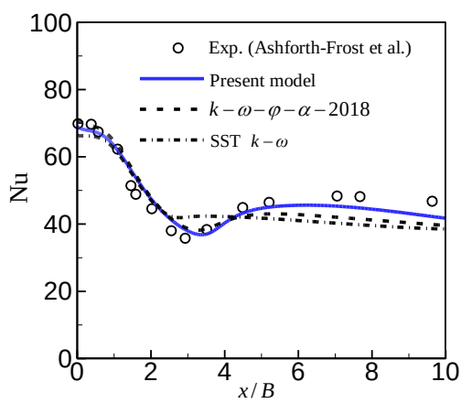

Figure 17.

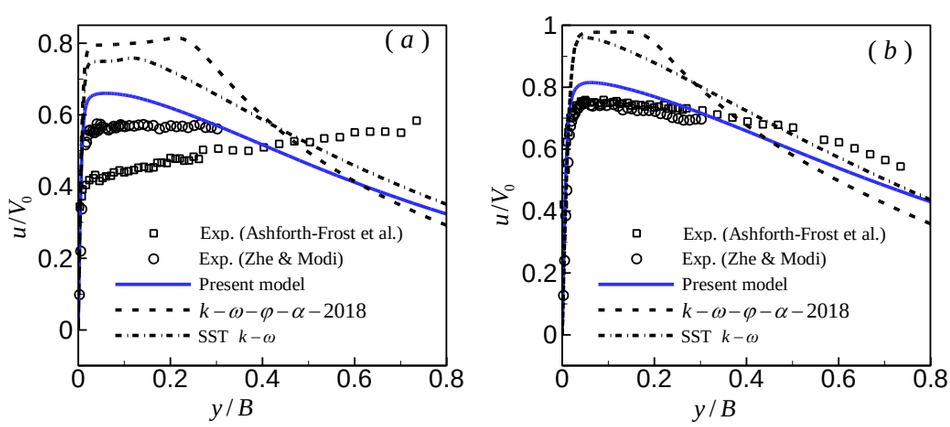

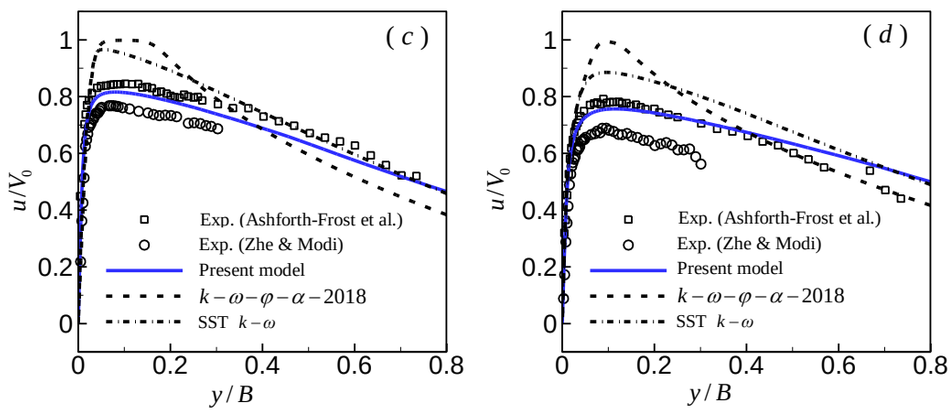

Figure 18.

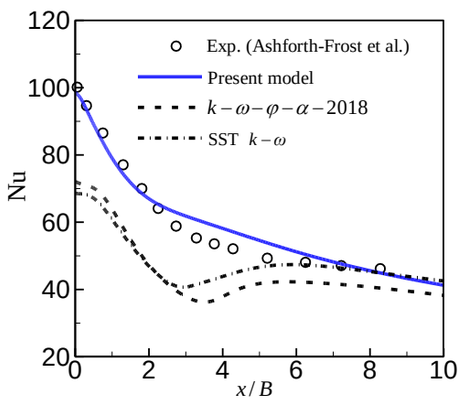

Figure 19.

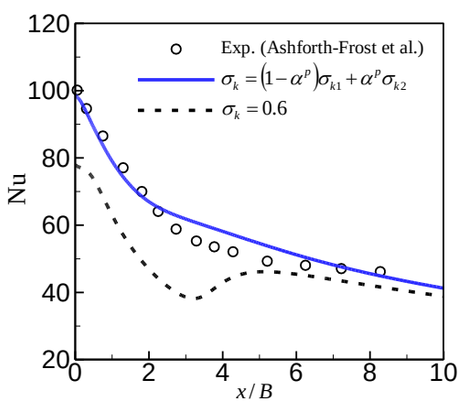

Figure 20.

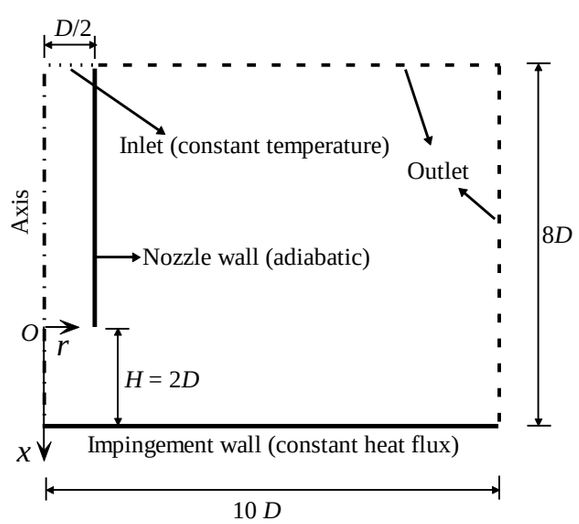

Figure 21.

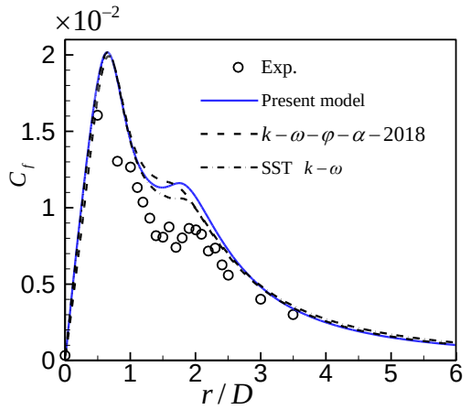

Figure 22.

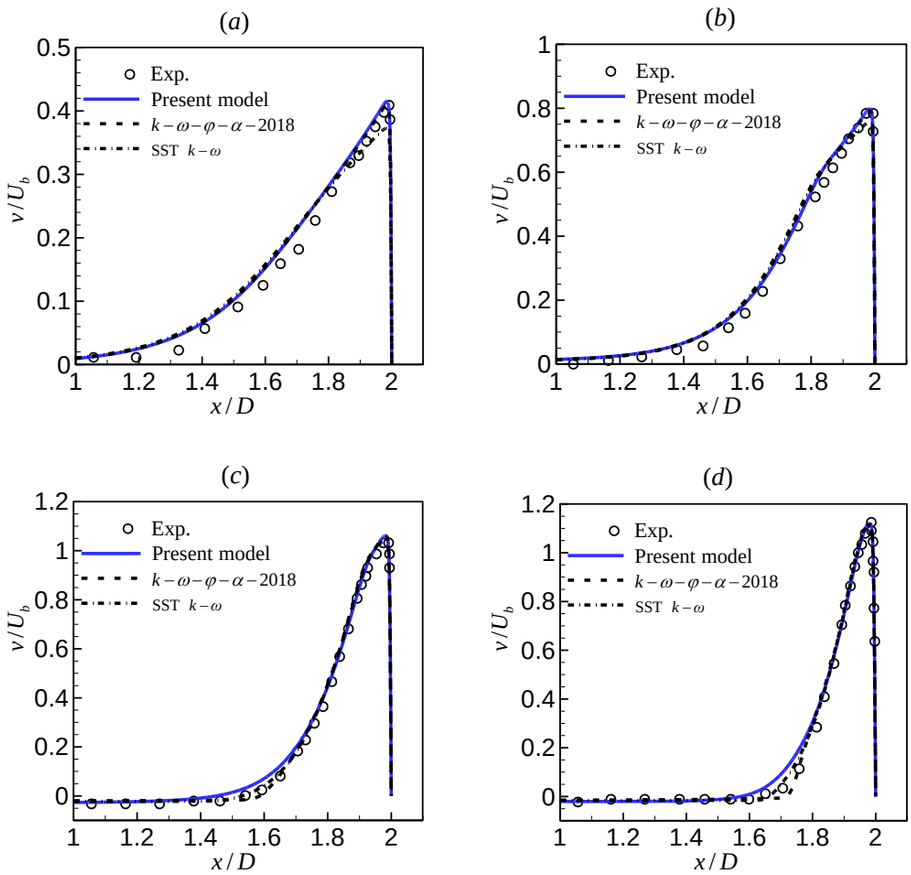

Figure 23.

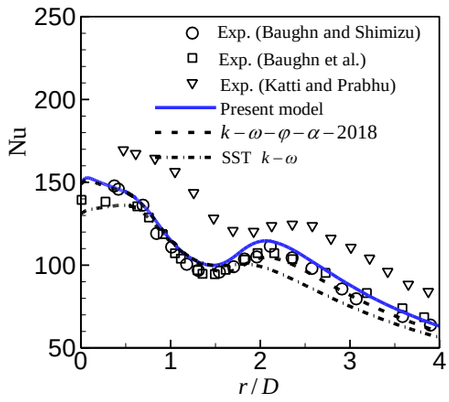
Exp. (Baughn and Shimizu)
Exp. (Baughn et al.)
Exp. (Katti and Prabhu)
Present model
$k-\omega-\varphi-\alpha-2018$
SST $k-\omega$
Nu
r/D
250
200
150
100
50
0
1
2
3
4

Figure 24.